

Article

Mechanical Properties and Acoustic Emission Characteristics of Unloading Instability of Sandstone under High Stress

Zhiyuan Hou ¹, Fukun Xiao ^{2,*}, Gang Liu ², Oleg Viktorovich Bashkov ³ and Lan Lyu ^{3,4}

¹ School of Safety Engineering, Heilongjiang University of Science and Technology, Harbin 150022, China; houzhizyuan0814@126.com

² Heilongjiang Ground Pressure & Gas Control in Deep Mining Key Lab, Heilongjiang University of Science and Technology, Harbin 150022, China; 18944630110@163.com

³ Institute of Mechanical Engineering and Chemical Technologies, Komsomolsk-na-Amure State University, 681013 Komsomolsk-na-Amure, Russia; bashkov@knastu.ru (O.V.B.); lvlan1980@163.com (L.L.)

⁴ International Cooperation and Exchanges Office, Heilongjiang University of Science and Technology, Harbin 150022, China

* Correspondence: xiaofukun@hotmail.com

Abstract: In order to analyze the law of unloading instability of deep rock mass, the unloading experiment of sandstone under different confining pressures was carried out, and the mechanical properties and acoustic emission characteristics of sandstone unloading failure under high stress were obtained. The results demonstrate that before unloading, the sandstone under low stress shows compression and elastic deformation, whereas that under high stress shows elastic deformation and plastic deformation. Moreover, the unloading behavior of sandstone under low stress is ductile, whereas that under high stress is brittle. Poisson's ratio and elastic modulus have negative and positive correlation with initial confining pressure, respectively. During unloading, the higher the initial confining pressure is, the earlier the rock sample damage occurs. Prior to the accelerated damage stage, the unloading amount and AE cumulative count are inversely proportional and directly proportional to the initial confining pressure, respectively. The simultaneous occurrence of UHF, HF, MF, and LF in the AE power spectrum, as well as a steep increase in fractal dimension followed by a decrease, can be used as precursors to unloading instability in sandstone.

Keywords: unloading instability; mechanical properties; acoustic emission characteristics; failure precursor



Citation: Hou, Z.; Xiao, F.; Liu, G.; Bashkov, O.V.; Lyu, L. Mechanical Properties and Acoustic Emission Characteristics of Unloading Instability of Sandstone under High Stress. *Minerals* **2022**, *12*, 722. <https://doi.org/10.3390/min12060722>

Academic Editors: Anye Cao, Zhenlei Li and Yosoon Choi

Received: 6 April 2022

Accepted: 1 June 2022

Published: 5 June 2022

Publisher's Note: MDPI stays neutral with regard to jurisdictional claims in published maps and institutional affiliations.



Copyright: © 2022 by the authors. Licensee MDPI, Basel, Switzerland. This article is an open access article distributed under the terms and conditions of the Creative Commons Attribution (CC BY) license (<https://creativecommons.org/licenses/by/4.0/>).

1. Introduction

As coal production in China increases, many Chinese coal mines have gone through the deep mining phase which features rockburst, water inrush, and high ground temperature. How to exploit deep coal resources safely and efficiently has become a challenge that the coal industry must tackle [1,2]. The excavation of roadway and large chambers is an unloading process of rock mass, which is completely different from the loading of rock mass. In particular, the stress state of deep rock mass development is more different [3–6]. Therefore, it is of great significance to study rock mass unloading under deep and high stress conditions to understand the failure mechanism of deep rock mass excavation.

The deformation instability of rock mass under the unloading path has attracted the attention of many scholars, and lots of research findings have been generated. In terms of the mechanical mechanism of rock unloading failure, Y. Han et al. [7] studied the mechanical behaviors of salt rock under different unloading rates, and defined the relationship between unloading rate and deformation parameters of rock specimens. Q. B. Meng et al. [8,9] discussed the energy evolution mechanism of rock loading and unloading conditions at high-temperature. I. Faoro et al. [10] investigated the permeability of high-temperature granites under the influence of unloading. H. G. Zhao et al. [11,12] conducted an experimental study

on the relationship between the permeability characteristics and the unloading rate of sandstone under the unloading path. A. Moslehy et al. [13,14] analyzed the change of porosity of salt rock and clay rock under unloading. V. Lyakhovskiy et al. [15] established a pore elastic model to describe the anisotropy of rocks based on triaxial cyclic loading and unloading. F. X. Passelegue et al. [16–18] discussed the damage of rock cycle after loading and unloading. G. Walton et al. [19] carried out an experimental study on the residual strength of rock under the unloading stress path. H. Sone et al. [20,21] analyzed the deformation of shale and sandstone under loading and unloading conditions, respectively. Y. J. Zhang et al. [22] carried out a numerical simulation study on marble with prefabricated cracks by using the three-dimensional discrete element method based on particles, and explored the impact of crack size, initial confining stress and unloading rate on the failure of rock specimens. A. Manouchehriyan et al. [23] used numerical simulations to discuss the energy transformation between the rock and the loading system in the unloading path. D. Hoxha et al. [24,25] studied the unloading creep in gypsum rocks and hard rocks and developed corresponding creep models. Since the acoustic emission characteristics of rock can efficiently characterize the failure, and as a result many scholars apply an acoustic emission technique to rock unloading studies. G. A. Zhu et al. [26–28] conducted an acoustic emission experiment on the true triaxial unloading failure of coal rock, and discussed the internal fracture and the evolution law of AE energy of coal specimens. S. Akdag et al. [29] carried out a true triaxial unloading test on brittle rocks and discussed the effect of thermal damage on rockbursts using acoustic emission b-values. Y. P. Liang et al. [30] defined the yield parameter based on the acoustic emission amplitude, and presented a discriminant method of precursor information based on yield parameters by the unloading experiment after the rock peak. X. H. Ni et al. [31] conducted an experiment and studied the acoustic emission characteristics of sandstone unloading after freeze-thaw cycles. M. C. He et al. [32,33] discussed the failure process of rock from the perspective of AE frequency, and found that acoustic emission showed high frequency and low amplitude under low stress, whereas it showed low frequency and high amplitude before failure. X. G. Zhao et al. [34] conducted an experimental study on hard rock with different unloading rates, and found that when the unloading rate is greater than 0.05 MPa/s, the cumulative energy of acoustic emission does not change significantly with the change of the unloading rate. G. Y. Hou et al. [35] discussed the impact of initial confining stress and unloading speed on rock failure, and believed that the widening of peak frequency and the increase in amplitude of the acoustic emission signal can be regarded as the precursor of a major crack. M. W. Zhang et al. [36,37] believed that the Felicity effect of rock in the elastic phase of rock deformation decreases as the unloading rate increases. D. X. Liang et al. [38,39] analyzed the Kaiser effect under cyclic loading and unloading on rocks, and found that the greater the rock hardness is, the earlier the Kaiser stress point appears. The Kaiser effect is more obvious under stepped cyclic loading. G. M. Zhao et al. [40–42] used an acoustic emission technique to analyze the damage evolution characteristics of rock under cyclic loading and unloading. K. Zhao et al. [43,44] conducted an experiment on the creep characteristics of rock under unloading, and established the unloading creep damage model based on acoustic emissions. The above scholars analyzed the mechanical properties of rock unloading by using the stress paths of unloading confining pressure under increasing axial pressure, cyclic loading and unloading. The mechanical characteristics of rock under different unloading rates were also analyzed. However, the stress path of underground rock mass excavation is complex, and the stress path of unloading confining pressure under constant axial pressure is not considered in the above research, especially the unloading problem of rock masses under high confining pressure. Therefore, it is necessary to study the stress path of unloading confining pressure in the case of constant axial pressure under high confining pressure. In the study of acoustic emission characteristics of rock unloading, scholars have discussed the changes of characteristic parameters such as b-value, amplitude and frequency, but the analysis of acoustic emission characteristics using the Welch power spectrum estimation method has not been reported.

In view of this, in order to grasp the unloading instability characteristics of deep rock mass, experimental research on the unloading of rocks under high confining pressure is needed. During the excavation process of underground engineering works, the rock mass on the side near the tunnel wall is more inclined to the state of constant vertical force and reduced lateral force, so the stress path of constant axial pressure and unloading confining pressure is chosen. In the following sections, firstly, the experimental methods and principles are introduced. Then, according to the stress and strain information monitored by the rock mechanics experimental system, the mechanical properties of unloading instability of rock masses under high confining pressure are analyzed. Finally, the unloading damage information and instability precursor information of rock masses under high confining pressure are analyzed from the aspects of acoustic emission count, power spectrum and fractal characteristics. The results of the study will help engineers to grasp the instability characteristics of deep rock masses.

2. Methods and Principles

2.1. Specimen Preparation

In this unloading experiment, homogeneous yellow sandstone was used as the experimental material. In accordance with the relevant International Society for Rock Mechanics and Rock Engineering (ISRM) standard, the sandstone was processed into standard ϕ 50mm \times 100 mm cylinder specimens with the unevenness error at both ends less than 0.05 mm. Next, the specimens were dried in a drying oven and were screened by the ultrasonic velocity measurement system with P-wave velocity of 3900 m/s and S-wave velocity of 3100 m/s, and a margin of error of 200 m/s. The screened samples are shown in Figure 1.



Figure 1. Screened sample.

2.2. Experimental System

The Rock600 press produced by the French company Top Industrie was chosen as the experimental system. The vertical pressure range of the press is 0–357 MPa, the lateral pressure range is 0–60 MPa, and the accuracy is 0.01 MPa. The acoustic emission monitoring device was the SH-II outdoor structural health monitoring system by (Physical Acoustics, Inc, Princeton, NJ, USA). The device is a 16-channel full-digital real-time acquisition system which can collect waveform flow and calculate characteristic parameters in real time, including acoustic emission amplitude, count, energy and impact. Depending on the frequency characteristics of the rock fracture signal, a Nano30 sensor was used. This has a resonant frequency of 300 kHz, and a working frequency of 100–450 kHz. The experimental system is shown in Figure 2 [45].

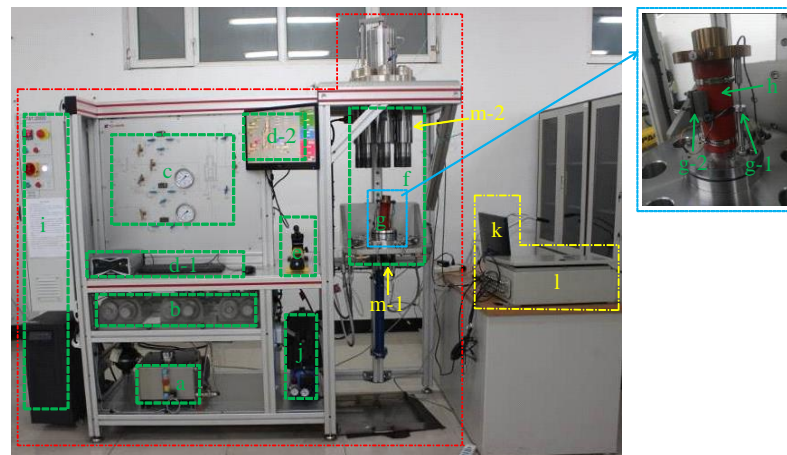


Figure 2. Experimental site. (a, b, e, f, g, j-loading system; c, d, i-control system; h-sample; k, l, m-acoustic emission system).

2.3. Experimental Protocol and Principle

The stress path selected in this paper is unloading confining pressure under constant axial pressure, as shown in Figure 3a. Four gradients of confining pressures, 10 MPa, 20 MPa, 30 MPa, and 40 MPa, are set during the experiments. The axial stress is 70% of the damage load of the rock sample under the current confining pressure, which are 105 MPa, 144 MPa, 188 MPa, and 225 MPa, respectively. Initially, the confining stress was elevated to the target value at the speed of 2 MPa/min, followed by the axial stress reaching the target value at the same speed. After the specimens were stabilized, the confining stress was reduced at the rate of 0.9 MPa per minute until they were damaged. During the experiment, acoustic emission signals were collected simultaneously. Acoustic emission was turned on when loading the axial stress (σ_1). The acoustic emission preamplifier was set at 40 dB, the acoustic emission threshold at 40 dB, the sampling frequency of the acoustic emission instrument at 1 MHz, and the sampling frequency of the waveform at 1 MSPS.

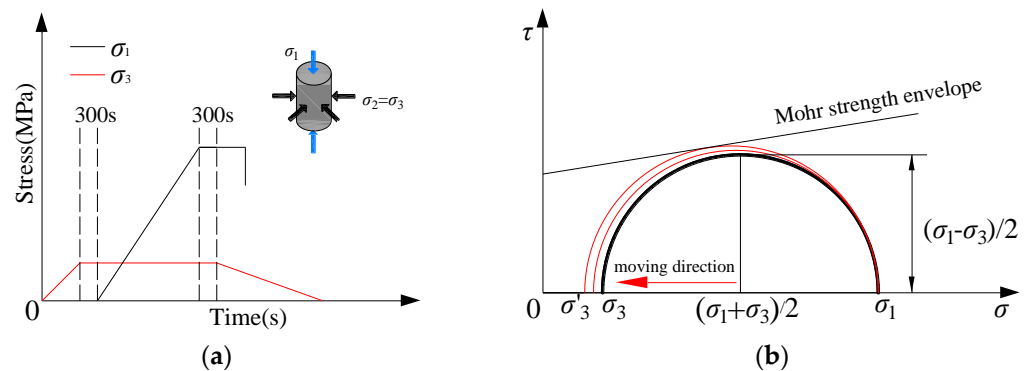


Figure 3. Experimental process and principle. (a) Stress process of rock specimen; (b) Experimental principle.

For the stress problem of subsurface rock masses, true triaxial experiments can well restore the stress state of the rock mass. It has been shown that the intermediate principal stress σ_2 has a certain effect on the damage of the rock [46]. The intermediate principal stress causes friction between the specimen and the pressure plate, and the friction changes the stress distribution within the specimen, which affects the damage process and peak strength. At the same time, the intermediate principal stress σ_2 increases the peak rock strength slightly if the frictional effect is neglected. Therefore, it is reasonable to adopt the Mohr-Coulomb criterion that simplifies the effect of σ_2 [23]. The Mohr-Coulomb criterion assumes that a combined force exists in the plane of each tiny unit inside the rock and can be equated to a positive stress (σ) and a shear stress (τ). Each group of positive stress (σ)

and shear stress (τ) is distributed on a circular arc with $(\sigma_1 + \sigma_3/2, 0)$ as the center and $\sigma_1 - \sigma_3/2$ as the radius. Rupture of the rock occurs when the stress circle is tangent to the strength envelope, as shown in Figure 3b. The black circle in the figure represents the initial stress state. When the confining pressure σ_3 decreases gradually, the center of the circle of stress will move to the left and the radius of the circle will increase until it is tangent to the strength envelope and the rock is damaged.

3. Analysis of Mechanical Characteristics of Sandstone Failure under Unloading Path

3.1. Failure Strength Characteristics

Figure 4 is the stress-strain curves of the specimen under confining stress release. $\sigma_1 - \sigma_3$ is partial stress, ε_1 is vertical strain, ε_3 is lateral strain and ε_v is the volume strain which compresses in the positive direction and expands in the negative direction. It can be seen from Figure 4a,b that there is a typical compaction phase (*oa* section) in the initial phase of loading where micropores between particles and microcracks in the rock specimen gradually close, and the slope of the curve becomes steep with the increase of displacement. As stress increases, the rock specimen enters the elastic deformation phase (*ab* section). Here the rock specimen exhibits good linear elasticity, the slope of the curve remains unchanged, and the internal elastic energy of the rock specimen gradually accumulates [47,48]. In Figure 4c,d, the axial strain at the initial phase of loading increases linearly with stress, and the rock specimen directly enters the elastic deformation phase (*ab* section), in which a large amount of internal elastic strain energy accumulates. As the stress continues to increase, the slope of the curve becomes gentle, internal microfractures in the specimen gradually increases, the overall stiffness gradually weakens, and the rock specimen enters the plastic deformation phase (*bc* section). By comparing the stress-strain curves of the rock specimen before the unloading point under each initial confining stress, it can be seen that under low stress ($\sigma_3 = 10$ MPa, $\sigma_3 = 20$ MPa), the rock specimen only undergoes compaction and elastic deformation, but not plastic deformation, while under high stress ($\sigma_3 = 30$ MPa, $\sigma_3 = 40$ MPa), the rock specimen undergoes elastic deformation and plastic deformation, but not compaction, and the higher the initial stress is, the more obvious the plastic deformation is. The main reason is that under low initial stress, the overall stiffness of the rock specimen is good, the damage is low, and there is no plastic flow. Under high initial stress, micropores between particles and microcracks in the rock specimen are compacted before loading, and as a result, compaction does not occur in the loading phase. As the initial stress increases, the overall stiffness of the rock specimen weakens greatly and microfractures develop significantly, exhibiting obvious plastic deformation. This phenomenon also implies that the internal damage of rock mass at low initial stress before unloading is low, whereas that at high stress before excavation is high. Therefore, close attention should be paid to the support of surrounding rock.

As unloading begins, the axial strain, radial strain and volume strain increase significantly. The radial expansion is significantly greater than the axial compression, the volume strain also changes from compression to expansion. Finally, the rock failure is manifested by volume expansion. Table 1 shows the mechanical characteristic parameters of the unloading failure of rock specimens, including initial confining stress (σ_{3i}), initial deviatoric stress ($\sigma_{1i} - \sigma_{3i}$), failure confining stress (σ_{3f}), residual deviatoric stress ($\sigma_{1r} - \sigma_{3r}$), axial strain increment from unloading point to failure point ($\Delta\varepsilon_1$), radial strain increment from unloading point to failure point ($\Delta\varepsilon_3$), and volume strain increment from unloading point to failure point ($\Delta\varepsilon_v$). The data can be obtained from the stress-strain curve, and the data in the table is the average of the experimental results of each group of rock specimens. From the strain increments of rock specimens under each initial confining stress, it can be seen that the axial strain increment ($\Delta\varepsilon_1$) is positively correlated with the initial confining stress, whereas the radial strain increment ($\Delta\varepsilon_3$) and volume strain increment ($\Delta\varepsilon_v$) hardly change with the initial confining stress. The failure strength of rock is positively correlated with the confining stress gradient. The failure loads of the rock specimens under each confining stress gradient are 1.80 MPa, 7.64 MPa, 18.60 MPa and 25.22 MPa respectively, and the

decreasing ranges of confining stress are 82.00%, 61.80%, 38.00% and 36.95%, respectively. It can be concluded that under low confining stress ($\sigma_3 = 10$ MPa, $\sigma_3 = 20$ MPa), the rock specimen can bear a large drop in confining stress, whereas under high confining stress ($\sigma_3 = 30$ MPa, $\sigma_3 = 40$ MPa), the confining stress borne by the rock specimen is limited, which indicates that the rock specimen has good ductility under less circumferential stress and obvious brittleness under more circumferential stress. This can also be proved by the phenomena observed in the experiment. An obvious crisp sound was heard when the failure of the rock specimen occurred under high confining stress. This property of sandstone also reminds us that more attention should be paid to controlling the reduction of confining stress in the process of deep rock mass excavation in order to prevent the sudden instability of rock mass.

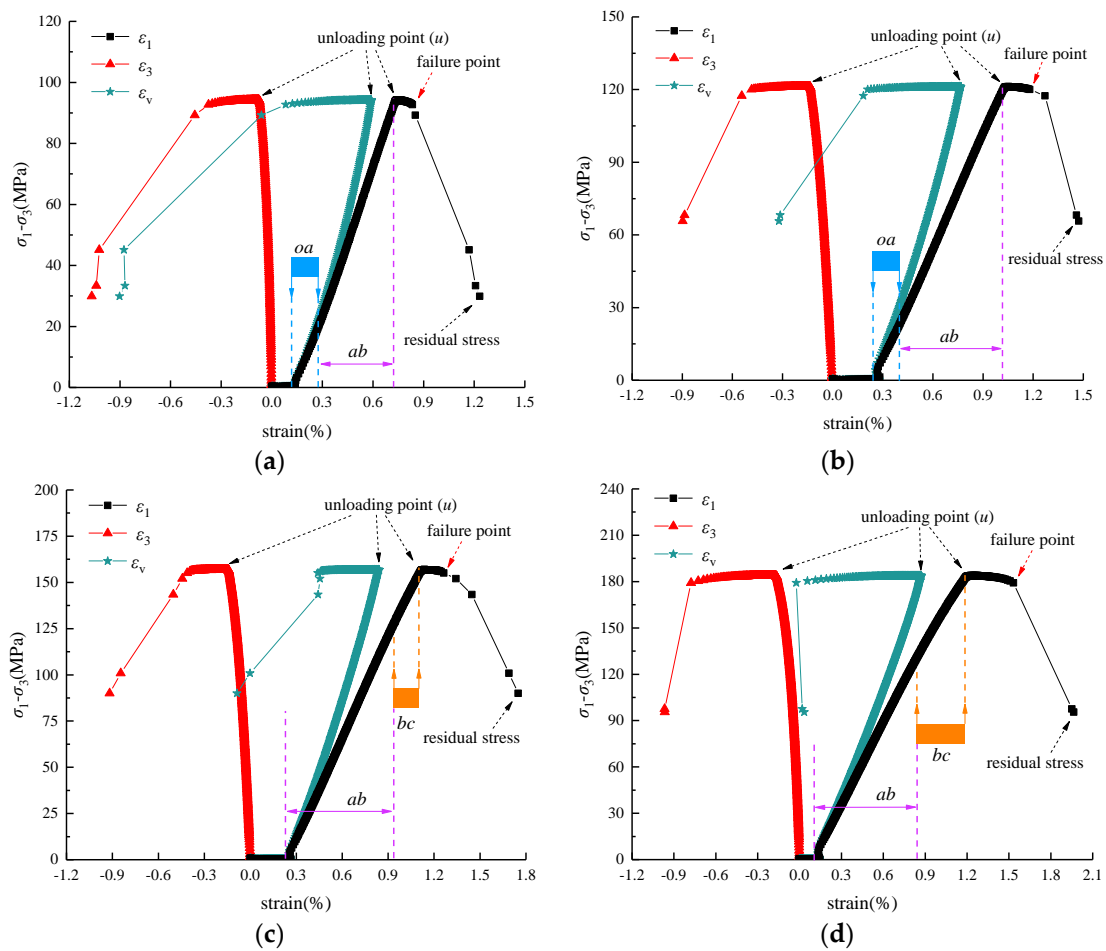


Figure 4. Stress-strain curves of sandstone unloading under different initial confining stresses. (a) $\sigma_3 = 10$ MPa; (b) $\sigma_3 = 20$ MPa; (c) $\sigma_3 = 30$ MPa; (d) $\sigma_3 = 40$ MPa.

Table 1. Mechanical parameters of sandstone unloading failure.

σ_{3i} (MPa)	$\sigma_{1i} - \sigma_{3i}$ (MPa)	σ_{3f} (MPa)	$\sigma_{1r} - \sigma_{3r}$ (MPa)	$\Delta\varepsilon_1$	$\Delta\varepsilon_3$	$\Delta\varepsilon_v$
10.00	95.00	1.80	28.55	0.105	−0.351	−0.596
20.00	121.00	7.64	63.97	0.201	−0.395	−0.589
30.00	157.00	18.60	78.63	0.230	−0.373	−0.516
40.00	184.00	25.22	97.25	0.248	−0.399	−0.549

Note: Data are average.

3.2. Characteristics of Failure Deformation of Sandstone under Unloading Path

In the unloading experiment, the increment of axial strain is less than that of radial strain. The secant method is used to calculate the Poisson’s ratio (μ), which is closer to

the real properties of the rock. The elastic modulus (E) can be obtained using the elastic formula. The calculation is shown in Formula (1) [49]:

$$\left. \begin{aligned} \mu &= \varepsilon_3 / \varepsilon_1 \\ E &= (\sigma_1 - 2\mu\sigma_3) / \varepsilon_1 \end{aligned} \right\} \quad (1)$$

Figure 5 shows the relationship between Poisson's ratio and confining stress of the sandstone after the unloading of sandstone under different confining stresses. It can be seen from the figure that the overall change of Poisson's ratio of rock specimens under each confining stress is consistent, that is, the Poisson's ratio increases with the decrease in confining stress. As unloading begins, the transverse restraint of the rock specimen gradually decreases and the radial expansion intensifies, which contributes to the increase in the Poisson's ratio. Poisson's ratio can reflect the expansion degree of the rock specimen during unloading. It should be noted that the lower the initial confining stress is, the greater the Poisson's ratio after unloading failure is, and the value is greater than the theoretical limit value of 0.5 for an elastic-plastic body. This shows that the expansion degree of the rock specimen under unloading failure is high under low confining stress, and Poisson's ratio greater than 0.5 indicates that the radial strain of the rock specimen contains some cracks, especially tensile cracks parallel to the axis, and the lower the confining stress is, the more developed the tensile cracks are. Figure 6 shows the relationship between elastic modulus and confining stress of sandstone unloading. The elastic modulus is positively correlated with the initial stress. Under the same strain, the rock specimen with greater elastic modulus stores more elastic strain energy, and releases more energy when being damaged. To sum up, during rock mass excavation under high stress, attention should be paid to controlling the deformation of surrounding rock to prevent sudden damage of rock mass.

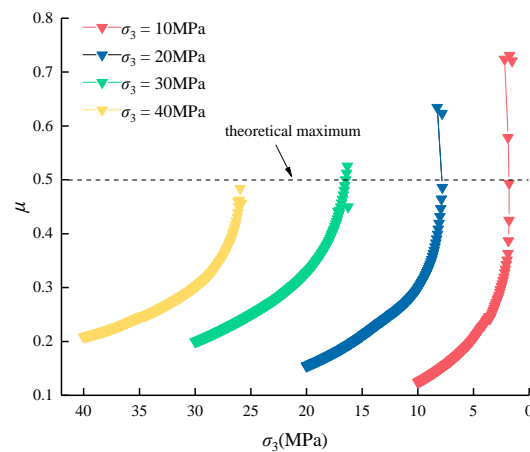


Figure 5. Relationship between Poisson's ratio and confining stress during unloading.

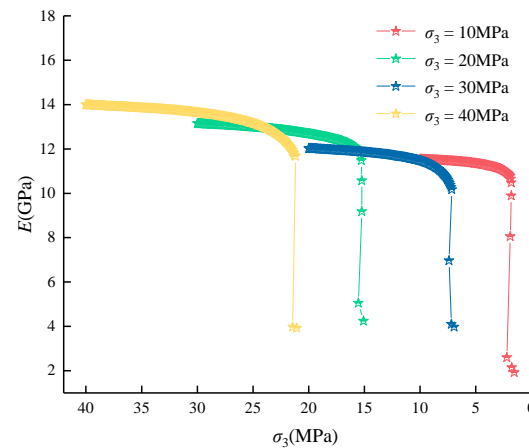


Figure 6. Relationship between elastic modulus and confining stress during unloading.

4. Analysis of Acoustic Emission Characteristics of Sandstone Failure under Unloading Path

4.1. Time Domain Characteristics of Acoustic Emission of Sandstone under Unloading Path

Through the research of scholars, it is found that the AE counts in time domain can better feedback the rock fracture information. The effect of confining stress gradient on AE information of rock sample unloading failure is obvious. The variation of ae count and stress with time under different confining stress gradients is shown in Figure 7. According to the characteristics of stress-time curve, the experimental process is divided into five phases: compaction phase (*oa*), elastic phase (*ab*), plastic phase (*bc*), maintenance phase (*cd*) and unloading phase (*de*). In Figure 7a,b, the activity of AE count in *oa* phase is low, and only particle compaction and crack closures occur in the rock specimens. In *ab* phase, the AE count appears constantly, the cumulative count increases linearly, and the rock specimen damage develops stably. In *cd* phase, the axial stress and confining stress remain constant, there are a few AE signals, and the damage degree of the rock specimen is low. In (*de*) phase, there is a blank period in AE count at the initial phase of unloading. At this point, the circumferential constraint decreases, the internal energy of the rock specimen is released, and the crack development stops for a short time. As the confining stress decreases, the activity of AE count gradually increases and the growth rate of cumulative count curve gradually increases, the rock specimen enters the accelerated damage phase, and a large number of internal fractures are developed. As the confining stress further decreases, a large number of high-count AE signals appear, and microcracks interconnects with each other to form macrocracks, which eventually leads to the instability and failure of the rock specimen and the release of ultra-high-count AE signals. Figure 7c,d show the experimental process of sandstone unloading under high stress. In the loading phase under high confining stress, the rock specimen does not undergo compaction, but directly enters the elastic deformation phase, in which the damage develops stably. The rock specimen then enters the *bc* phase, in which the AE count distribution gradually becomes dense, the activity degree gradually increases, and the damage development accelerates. AE counts in *cd* phase are dense and then sparse. At this point, the energy dissipation in the rock specimen gradually decreases and the crack development gradually slows down. At the beginning of *de* phase, there is a short blank period for AE count, and the higher the initial confining stress is, the shorter the duration of the blank period is. As the confining stress continue to decrease, the AE count distribution gradually becomes dense, and the count rate increases gradually until a large number of ultra-high AE counts are released due to the instability and failure of the rock specimen. Through side-by-side comparison the AE counting characteristics of sandstone failure under different initial confining stresses, in the loading phase, and under low initial confining stress ($\sigma_3 = 10$ MPa, $\sigma_3 = 20$ MPa), the AE count distribution shows obvious compaction and elastic deformation, while under high confining stress ($\sigma_3 = 30$ MPa, $\sigma_3 = 40$ MPa), the AE count distribution shows elastic deformation and plastic deformation, which is consistent with the characteristics of stress-

strain curve in Section 3.1. This also demonstrates that under high stress, the internal damage degree of sandstone before unloading is higher than that under low stress, as stated in the previous section. In the maintenance phase, cracks do not develop in the rock specimen under low confining stress, while under high confining stress, the elastic energy is released in the rock specimen, which is manifested by the gradual slow-down of the crack development. In the unloading phase, the higher the initial surrounding rock is, the shorter the blank period of AE count is, and the subsequent count distribution is denser, indicating that the higher the confining stress is, the earlier the unloading damage of the rock specimen occurs. This suggests that the deep rock mass excavation should be supported in time.

In Figure 7, the AE count continues to increase steadily within the range of phase I, the cumulative count curve becomes steeper, and a large number of high-count signals appear before the fracture of the rock specimen. Therefore, phase I is defined as the accelerated damage phase. Phase II is AE counts after rock specimen fracture. In this phase, high, medium and low AE counts are evenly distributed, and ultra-high counts caused by secondary fracture after peak appear. There are negative correlations between unloading amount and confining stress gradient in the accelerated damage phase, which are 63.20%, 52.45%, 38.70% and 20.80%, respectively. AE accumulative count ratio is positively correlated with confining stress gradient, which is 0.85%, 2.36%, 3.83% and 11.46%, respectively. It can be seen that the larger the initial stress is, the smaller the allowable unloading amount of the rock specimen is and the larger the AE cumulative count ratio is, indicating that the allowable unloading amount of deep rock mass excavation is smaller and the damage of rock mass is more serious before accelerated damage. The unloading percentage and cumulative count percentage under each initial confining stress can be used as the criteria to judge whether the rock has entered the accelerated damage phase, but the specific situation should also be taken into consideration for a comprehensive judgment.

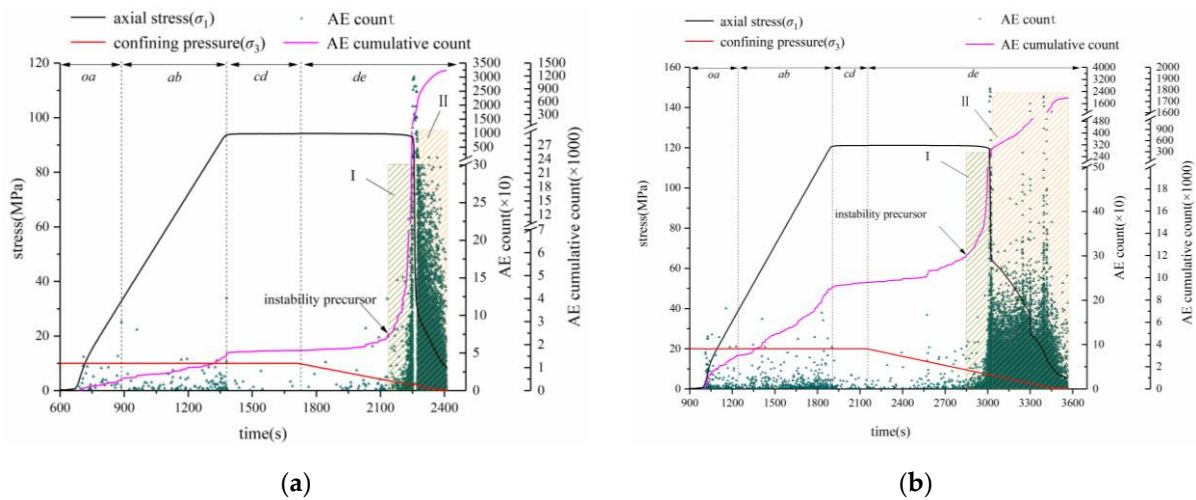


Figure 7. Cont.

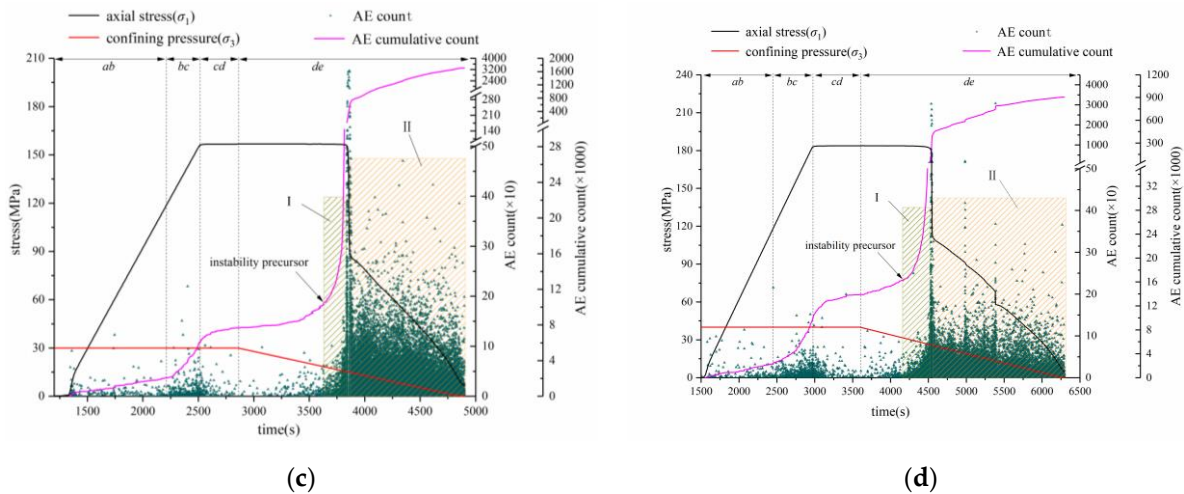


Figure 7. Stress-AE counting relationship of samples. (a) $\sigma_3 = 10$ MPa; (b) $\sigma_3 = 20$ MPa; (c) $\sigma_3 = 30$ MPa; (d) $\sigma_3 = 40$ MPa.

4.2. Frequency Domain Characteristics of Acoustic Emission of Sandstone under Unloading Path

AE signals not only reflect the important information of rock specimen fracture in the time domain, but also carry the spectral characteristics of rock specimen fracture in the frequency domain. Welch’s method for estimating power spectra is used to obtain a Fourier transform by overlapping and intersecting the data in segments, which can effectively compensate for the effect of data amount on the result in power spectrum analysis [50].

Segment handling of the data is performed, as shown in Formula (2):

$$L = \frac{N - \frac{M}{2}}{\frac{M}{2}} = \frac{2N - M}{M} \tag{2}$$

where: L is the number of segments; N is the data segment; M is the data point of each segment. Add window to the data segment and calculate the Fourier transform:

$$X(e^{j\omega}) = \sum_{n=0}^{M-1} X_i(n)\omega(n)e^{j\omega n}, (i = 1, 2, \dots, L) \tag{3}$$

Calculate the average value of power for each phase:

$$S_X(e^{j\omega}) = \frac{1}{L} \sum_{i=1}^L \frac{1}{U_M} |X_i(e^{j\omega})|^2 \tag{4}$$

where: U is the average power of window function; U_M is the energy of function $\omega(n)$ of M long window.

Figure 8 shows the distribution of peak frequency with time under different initial confining stresses. The peak frequency is characterized by the distribution of low frequency, intermediate frequency and several high frequencies. Based on the stress state of the rock specimen, the process is divided into loading phase (*ob, ac*), maintenance phase (*cd*), and unloading phase (*de*). The peak frequency in different phases exhibits different distribution characteristics. At the initial confining stress of 10 MPa, the peak frequency in the loading phase falls within the intermediate frequency range of 134~150 kHz, with a very small amount of low frequency (67 kHz) and ultra-high frequency (321 kHz) signals, and a small amount of intermediate frequency signals in the maintenance phase. In the initial phase of unloading, a small amount of intermediate frequency damage signals appears and internal damage develops stably in the rock specimen. As the confining stress further decreases, the intermediate frequency distribution range gradually widens,

and high frequency (237 kHz) and ultra-high frequency (347 kHz) signals appear. The internal damage of rock specimens enters the phase of unstable development, and high, medium and low frequency signals are released at the same time before failure [51]. At the initial confining stress of 20 MPa, the peak frequency distribution characteristics in the loading phase and maintenance phase are consistent with those shown in Figure 8a, with only a few high-frequency and low-frequency signals. Most signals are concentrated in the middle frequency band, and the rock specimen damage develops stably. At the initial phase of unloading, there are a large number of intermediate frequency signals and very few high-frequency signals. With the continuous reduction of confining stress, the intermediate frequency distribution range widens, and low-frequency (67 kHz) and high-frequency (240 kHz) signals begin to appear. Before failure, the peak frequency signal suddenly changes and an ultra-high frequency (345 kHz) signal appears. At the initial confining stress of 30 MPa, the peak frequency in the loading phase is mainly distributed in the middle frequency range of 134~155 kHz. At the end of the phase, a small amount of low-frequency, high-frequency, and ultra-high-frequency signals appear, and the rock specimen damage is in the unstable development phase. A large number of intermediate frequency signals appear in the maintenance phase. At the initial phase of unloading, a large number of intermediate frequency signals appear. With the continuous reduction of confining stress, the distribution range of intermediate frequency further widens, and a large number of low-frequency and high-frequency signals begin to appear. Before failure, ultra-high-frequency, high-frequency, intermediate frequency and low-frequency signals appear at the same time. At the initial confining stress of 40 MPa, the peak frequency in the loading phase is mainly distributed in the middle frequency band, with a small amount of low-frequency and high-frequency signals. In the maintenance phase, the width of intermediate frequency distribution narrows. The development of fractures releases the energy in the rock specimen and slows down the development of damage. At the initial phase of unloading, a large number of intermediate frequency signals also appear, and the intermediate frequency distribution further widens. A large number of high-frequency and low-frequency signals begin to appear, and ultra-high-frequency, high-frequency, intermediate frequency and low-frequency signals appear at the same time before failure.

From the above analysis, the higher the initial confining stress is, the more the number of high-frequency and low-frequency signals and the wider the distribution range is in the loading, maintenance and unloading phases. The peak frequency fluctuation of high-frequency signals is more intense than that of low-frequency signals. The generation of small-scale cracks in rock specimens corresponds to the formation of high-frequency signals, whereas the generation of large fractures corresponds to the formation of low-frequency signals, indicating that in the unloading process, the larger the confining stress is, the more complex is the development of internal cracks in the rock specimens. The formation of internal small cracks is random, whereas the formation of large fractures has certain commonalities. The distribution characteristics of high-frequency and low-frequency signals also indirectly show that the higher the confining stress is, the greater is the damage degree of rock specimen in the maintenance phase and the more severe is the damage in the unloading phase. Under each initial confining stress, the peak frequency signal before failure suddenly changes, and ultra-high frequency, high frequency, intermediate frequency and low frequency signals appear at the same time, indicating the coexistence of high and low frequency bands. It shows that the fracture of the rock specimen is the evolution process of microcrack initiation, propagation and penetration, and finally the formulation of large cracks, and the evolution of cracks in each phase is synchronous before failure. Therefore, the widening of intermediate frequency distribution, the sudden change of peak frequency, and the simultaneous occurrence of ultra-high frequency, high frequency, intermediate frequency, and low frequency signals can be used as the precursors of the rock specimen's instability.

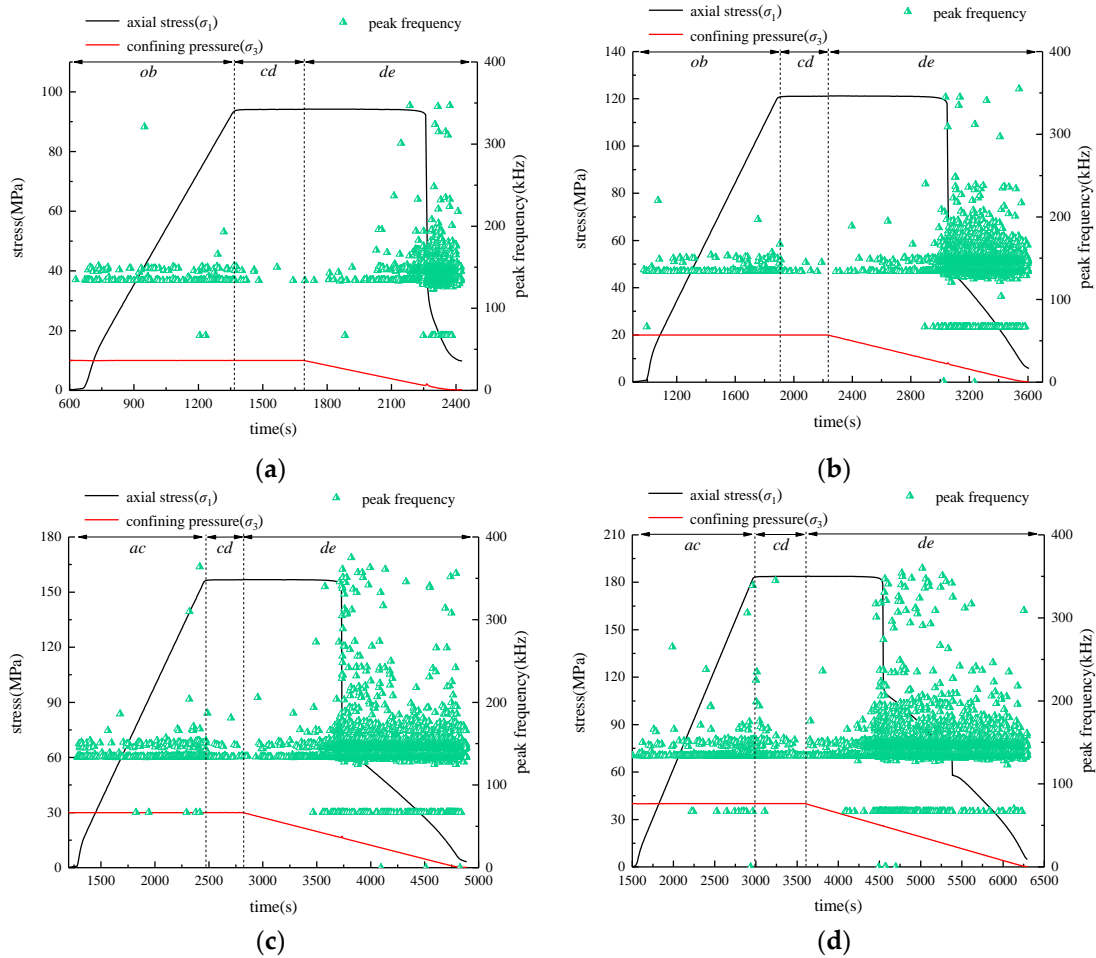


Figure 8. Peak frequency-stress-time relationship of sandstone unloading under different initial confining stresses. (a) $\sigma_3 = 10$ MPa; (b) $\sigma_3 = 20$ MPa; (c) $\sigma_3 = 30$ MPa; (d) $\sigma_3 = 40$ MPa.

4.3. Fractal Characteristics of Acoustic Emission of Sandstone under Unloading Path

To further analyze the unloading failure characteristics of sandstone, the fractal dimension of the AE signal is quantitatively analyzed. The delay-coordinate state space reconstruction assumes that the relationship between the dimension m of the delay coordinate and the sequence dimension d is $m \geq 2d + 1$, and the calculation process is based on the G-P algorithm [52], that is, the AE intensity of a single rock specimen during the test is taken as the sequence set with capacity n :

$$X = \{x_1, x_2, \dots, x_n\} \tag{5}$$

Take m numbers that can be juxtaposed in the sequence as the first vector of m -dimensional space,

$$Y_1 = \{x_1, x_2, \dots, x_m\} \tag{6}$$

Next, take m numbers in turn to form the second vector,

$$Y_2 = \{x_2, x_3, \dots, x_{m+1}\} \tag{7}$$

forming $N = n - m + 1$ vectors. According to the Takens theorem, the cumulative distribution function $W(r)$ of the probability that the distance between two points in space is less than r is obtained, as shown below:

$$W(r) = \frac{1}{N^2} \cdot \sum_{i,j}^N u(r - |Y_i - Y_j|) \quad (8)$$

where, u is the Heaviside function,

$$u(r - |Y_i - Y_j|) = \begin{cases} 1 & (u(r - |Y_i - Y_j|) \geq 0) \\ 0 & (u(r - |Y_i - Y_j|) < 0) \end{cases} \quad (9)$$

$|Y_i - Y_j|$ is the distance between the spatial phase points Y_i and Y_j , and r is the measurement scale. Through the linear fitting of data points $(\lg W(r), \lg r)$, the slope $D(m)$, which is the fractal feature of acoustic emission, is obtained, as shown below:

$$D(m) = \lg W(r) / \lg r \quad (10)$$

The AE data of the failure process of the rock specimen is calculated using MATLAB software. The AE fractal dimension (D) under different initial confining stresses is shown in Figure 9. AE fractal dimension can quantitatively describe the law of crack development in rock. At the initial phase of axial compression loading, the AE fractal dimension of the rock specimen under the confining stress of 10 MPa and 20 MPa shows a downward trend, and whereas that under the confining stress of 10 MPa and 20 MPa remains unchanged. The reason is that at the initial phase of loading, the rock specimen under low initial confining stress exhibits compaction and elastic deformation, pores and microcracks of varied sizes are compacted in the compaction phase, and the disorderliness of AE signals in the elastic phase is greater than that in the compaction phase, resulting in decreased fractal dimension. Under high initial confining stress, the rock specimen only exhibits elastic deformation in the initial phase of loading. In the elastic phase, cracks develop stably in the rock specimen, and the AE fractal dimension remains constant. In the middle and late phases of loading, the AE fractal dimension of the rock specimen under each initial confining stress gradually increases, and the greater the confining stress is, the greater the increase is. This shows that the internal crack development of the rock specimen gradually changes from orderly development to disorderly development, and the higher the initial confining stress is, the greater the degree of disorderly crack development is and the more serious the damage of rock specimen is. The AE fractal dimension under each initial confining stress in the maintenance phase decreases significantly. It is worth noting that the fractal dimension under low initial confining stress in the maintenance phase nearly reaches 0, whereas that under high initial confining stress is about 0.1, indicating that no damage occurs in the rock specimen under low confining stress in the maintenance phase, whereas slow damage appears in the rock specimen under high confining stress. At the initial phase of unloading, the AE fractal dimension of the rock specimen decreases under high initial confining stress, and changes horizontally under low initial confining stress. This is because at the initial phase of unloading, the circumferential constraint suddenly decreases, the energy in the rock specimen is released, and the crack development slows down, resulting in decreased fractal dimension. Under low initial confining stress, the circumferential constraint of rock specimens is low, the accumulated energy in rock specimens is low, and the crack development degree is low under the action of the rock specimen's stiffness at the initial phase of unloading, and as a result, the fractal dimension remains unchanged. With the continuous decrease of confining stress, the fractal dimension under each confining stress shows an upward trend, and the higher the confining stress is, the greater the increase in range and speed is, indicating that the cracks in the rock specimen at this phase are in a disorderly and accelerated development state, and the larger the confining stress is, the greater the crack development scale, degree and range. Before the failure of the rock

specimen, the cracks penetrate each other and expand in a common direction, develop from disorderly development to orderly development, and gradually form a shear zone; the fractal dimension decreases greatly, forming a fracture surface, and the brittle failure of the sample occurs rapidly. Therefore, the decrease in the AE fractal dimension of the rock specimen after a sharp increase in the unloading phase can be regarded as the precursor of the rock specimen's failure.

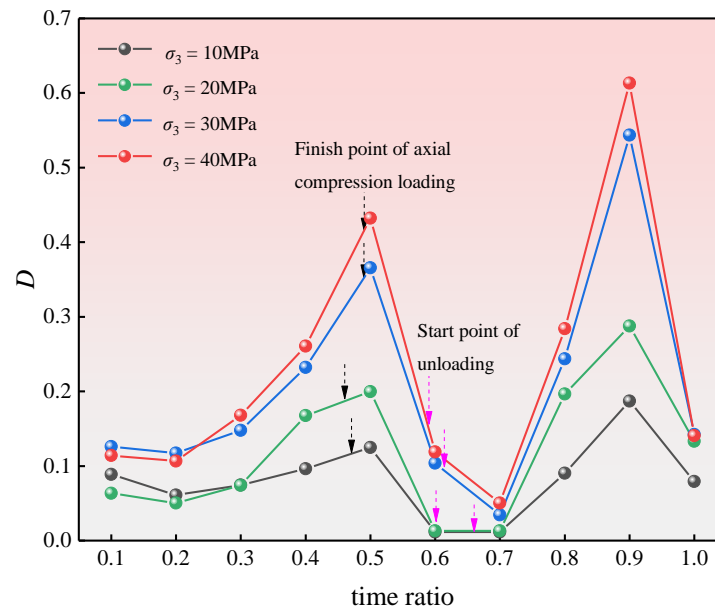


Figure 9. Variation curve of AE fractal dimension.

5. Discussion

Before unloading, rock masses under low confining pressure show compaction and elastic deformation, whereas rock masses under high confining pressure show elastic deformation and plastic deformation (see Figure 4). Compared with the elastic deformation, the internal fracture development is faster and the damage development is greater during the plastic deformation of the rock. After unloading, the initial confining pressure increased from 10 MPa to 40 MPa, and the corresponding axial strain increment $\Delta\varepsilon_1$ increased by 136.19%. In the unloading process, both the axial strain increment and the elastic modulus of rock masses increased with the increase of initial confining pressure, which is consistent with the reports of S. Wang et al. [9,12]. The radial strain increment $\Delta\varepsilon_3$ and the bulk strain increment $\Delta\varepsilon_v$ during rock sample unloading do not vary much with the initial confining pressure. The unloading amount is defined as the percentage of rock unloading from the beginning to the failure of confining pressure. The unloading amount is 82.22% at the initial confining pressure of 10 MPa and 36.95% at the initial confining pressure of 40 MPa. It can be seen that the unloading amount of rock masses with high confining pressure is much smaller than that with low confining pressure, and the unloading amount is inversely proportional to the initial confining pressure. The above law shows that the degree of damage before excavation of deep rock is greater than that of shallow rock, the allowable unloading amount is much smaller than that of shallow rock, and the damage of deep rock is shown as brittle damage. Therefore, deep rock excavation is more prone to rockburst and other dynamic disaster accidents, so the surrounding rock should be timely supported to control the reduction of the confining pressure to prevent disasters.

Acoustic emission counts provide a better feedback of rock damage in the time domain. At the beginning of loading, the cracks in the rock are compacted and the AE counts are low; then with the continuous increase in stress, the damage starts to occur and the AE counts become more and more active, as also found by M. C. He et al. [32,34,35] in their experiments. The higher the initial confining pressure before unloading, the denser the

distribution of AE counts and the greater the degree of damage in the rock samples. This again indicates that the degree of damage before excavation is higher in the deep rock than in the shallow rock. It is worth noting that the AE counts do not appear immediately when the confining pressure decreases in the unloading stage (*de*), and there is a certain lag effect, indicating that the rock has a certain bearing capacity at the early stage of unloading and can resist the occurrence of damage. However, the higher the initial confining pressure, the shorter the lag time of AE count, which demonstrates that the damage of deep rock mass occurs earlier than that of shallow rock mass, and support should be carried out as early as possible in the construction process. The peak frequency and fractal dimension of acoustic emission can judge the damage of rock from frequency domain and order degree, respectively. Before rock failure, the peak frequency suddenly changes and the fractal dimension greatly increases, which has potential application value in monitoring and early warning of underground rock excavation stability.

6. Conclusions

In this paper, an unloading experiment is carried out on sandstone, the mechanical properties of sandstone unloading failure under different initial confining stresses are discussed, and the unloading damage evolution characteristics of sandstone are analyzed from the time domain, frequency domain and fractal characteristics of acoustic emission. The following conclusions could be drawn from the experiments:

- (1) Under low stress, sandstone only exhibits compaction and elastic deformation before unloading, whereas under high stress, it exhibits elastic deformation and plastic deformation before unloading; axial strain increment ($\Delta\varepsilon_1$) is positively correlated with initial confining stress, whereas radial strain increment ($\Delta\varepsilon_3$) and volume strain increment ($\Delta\varepsilon_v$) are insensitive to the rise of initial confining stress; the unloading failure of the rock specimen shows good ductility under low confining stress and obvious brittleness under high confining stress.
- (2) The Poisson's ratio of unloading failure of the rock specimen is inversely related to the initial confining stress. The lower the initial confining stress is, the more serious the expansion of the rock specimen after failure is; the elastic modulus is directly proportional to the initial confining stress, and the higher the initial confining stress is, the higher the elastic strain energy stored in the rock specimen is.
- (3) The higher the initial confining stress in the unloading phase (*de*) is, the shorter the duration of the blank period of AE count is, and the earlier the damage appears; under different initial confining stresses, the AE count of the rock specimen increases sharply before failure, and the unloading failure of the rock specimen is more sudden.
- (4) Before entering the accelerated damage phase, the unloading amount of confining stress is inversely proportional to the initial confining stress, and the AE cumulative count ratio is directly proportional to the initial confining stress; the excavation unloading of the high stress rock mass enters the accelerated damage phase earlier and the damage is more serious.
- (5) Under each initial confining stress, the AE power spectrum frequency of the rock specimen in the loading phase is mainly distributed in the intermediate frequency range of 134~155 kHz. After unloading, the intermediate frequency distribution gradually widens, and low frequency and high frequency signals begin to appear. Ultra-high frequency, high frequency, intermediate frequency and low frequency occur simultaneously before the rock specimen's failure, which can serve as the precursors of the rock specimen's instability.
- (6) AE fractal dimension can better reflect the orderliness and disorderliness of AE signals in the unloading process of the rock specimen, and the downward trend after the sharp increase in fractal dimension can serve as the precursor of the rock specimen's failure.

Author Contributions: Conceptualization, Z.H. and F.X.; Methodology, Z.H.; Software, Z.H.; Validation, Z.H. and L.L.; Formal Analysis, G.L. and O.V.B.; Investigation, Z.H.; Resources, F.X.; Data Curation, Z.H.; Writing-Original Draft Preparation, Z.H.; Writing-Review and Editing, Z.H. and G.L.; Visualization, Z.H.; Supervision, O.V.B.; Project Administration, F.X.; Funding Acquisition, F.X. All authors have read and agreed to the published version of the manuscript.

Funding: The research was funded by the Natural Science Foundation of Heilongjiang Province (Grant no. ZD2021E006).

Institutional Review Board Statement: Not applicable.

Informed Consent Statement: Not applicable.

Data Availability Statement: Not applicable.

Acknowledgments: The authors would like to thank all members for their help with the fieldwork in Heilongjiang Ground Pressure & Gas Control in Deep Mining Key Lab (GPGC).

Conflicts of Interest: The authors declare no conflict of interest.

References

- Zhao, S.K.; Qi, Q.X.; Li, Y.P.; Deng, Z.G.; Li, Y.Z.; Su, Z.G. Theory and Practice of Rockburst Stress Control Technology in Deep Coal Mine. *J. China Coal Soc.* **2020**, *45*, 626–636.
- Lan, H.; Chen, D.K.; Chen, D.B. Current Status of Deep Mining and Disaster Prevention in China. *Coal Sci. Technol.* **2016**, *41*, 39–46.
- Jia, P.; Yang, N.; Liu, D.Q. Effect of Unloading Direction on Rock Failure under True Triaxial Stress Conditions. *J. Test. Eval.* **2021**, *49*, 4058–4071. [[CrossRef](#)]
- Luo, Y.; Huang, J.H.; Lu, W.B.; Zhang, G.; Li, X.P.; Song, K.W. Study on Transient Unloading Loosening Simulation Test of Excavation of Jointed Rock Mass. *Proc. Inst. Civ. Eng.-Geotech. Eng.* **2021**, *147*, 645–656. [[CrossRef](#)]
- Zhao, Y.; Wang, C.L.; Bi, J. Analysis of Fractured Rock Permeability Evolution under Unloading Conditions by the Model of Elastoplastic Contact Between Rough Surfaces. *Rock Mech. Rock Eng.* **2020**, *53*, 5795–5808. [[CrossRef](#)]
- Yang, Y.Z.; Zhang, Z.N. Surrounding Rock Effect on Coal Burst under Unloading Condition: a Numerical Study. *Arab. J. Geosci.* **2021**, *14*, 1742. [[CrossRef](#)]
- Han, Y.; Ma, H.L.; Yang, C.H.; Li, H.; Yang, J. The mechanical behavior of rock salt under different confining pressure unloading rates during compressed air energy storage (CAES). *J. Pet. Sci. Eng.* **2021**, *196*, 107676. [[CrossRef](#)]
- Meng, Q.B.; Liu, J.F.; Huang, B.X.; Pu, H.; Wu, J.Y.; Zhang, Z.Z. Effects of Confining Pressure and Temperature on the Energy Evolution of Rocks under Triaxial Cyclic Loading and Unloading Conditions. *Rock Mech. Rock Eng.* **2022**, *55*, 773–798. [[CrossRef](#)]
- Wang, S.; Wang, H.; Xu, W.; Qian, W. Investigation on mechanical behaviour of dacite under loading and unloading conditions. *Geotech. Lett.* **2019**, *9*, 130–135. [[CrossRef](#)]
- Faoro, I.; Vinciguerra, S.; Marone, C.; Elsworth, D.; Schubnel, A. Linking permeability to crack density evolution in thermally stressed rocks under cyclic loading. *Geophys. Res. Lett.* **2013**, *40*, 2590–2595. [[CrossRef](#)]
- Zhao, H.G.; Liu, C.; Huang, G. Dilatancy Behaviour and Permeability Evolution of Sandstone Subjected to Initial Confining Pressures and Unloading Rates. *R. Soc. Open Sci.* **2021**, *8*, 201792. [[CrossRef](#)] [[PubMed](#)]
- Liu, S.L.; Zhu, Q.Z.; Shao, H.F. Deformation and Mechanical Properties of Rock: Effect of Hydromechanical Coupling under Unloading Conditions. *Bull. Eng. Geol. Environ.* **2020**, *79*, 5517–5534. [[CrossRef](#)]
- Moslehy, A.; Alshibli, K. Assessment of the properties of polycrystalline rock salt synthesized under nominally dry and wet conditions. *J. Rock Mech. Geotech. Eng.* **2021**, *13*, 311–320. [[CrossRef](#)]
- Delage, P.; Menaceur, H.; Tang, A.M.; Talandier, J. Suction effects in deep Callovo-Oxfordian claystone. *Geotech. Lett.* **2014**, *4*, 267–271. [[CrossRef](#)]
- Lyakhovskiy, V.; Panteleev, I.; Shalev, E.; Browning, J.; Mitchell, T.M.; Healy, D.; Meredith, P.G. A new anisotropic poroelasticity model to describe damage accumulation during cyclic triaxial loading of rock. *Geophys. J. Int.* **2022**, *230*, 179–201. [[CrossRef](#)]
- Passelegue, F.X.; Pimienta, L.; Faulkner, D.; Schubnel, A.; Fortin, J.; Gueguen, Y. Development and Recovery of Stress-Induced Elastic Anisotropy During Cyclic Loading Experiment on Westerly Granite. *Geophys. Res. Lett.* **2018**, *45*, 8156–8166. [[CrossRef](#)]
- Taheri, A.; Yfantidis, N.; Olivares, C.L.; Connelly, B.J.; Bastian, T.J. Experimental Study on Degradation of Mechanical Properties of Sandstone Under Different Cyclic Loadings. *Geotech. Test. J.* **2016**, *39*, 20150231. [[CrossRef](#)]
- Munoz, H.; Taheri, A. Postpeak Deformability Parameters of Localized and Nonlocalized Damage Zones of Rocks under Cyclic Loading. *Geotech. Test. J.* **2019**, *42*, 1663–1684. [[CrossRef](#)]
- Walton, G.; Gaines, S.; Alejano, L.R. Validity of continuous-failure-state unloading triaxial tests as a means to estimate the residual strength of rocks. *J. Rock Mech. Geotech. Eng.* **2021**, *13*, 717–726. [[CrossRef](#)]
- Sone, H.; Zoback, M.D. Mechanical properties of shale-gas reservoir rocks—Part 1: Static and dynamic elastic properties and anisotropy. *Geophysics* **2013**, *78*, D378–D389. [[CrossRef](#)]

21. Alvarado, G.; Coop, M.R.; Willso, S. On the role of bond breakage due to unloading in the behaviour of weak sandstones. *Geotechnique* **2012**, *62*, 303–316. [[CrossRef](#)]
22. Zhang, Y.J.; Liu, S.J.; Kou, M.M.; Wang, Z.Q. 3-D Numerical Study on Progressive Failure Characteristics of Marbles under Unloading Conditions. *Appl. Sci.* **2020**, *10*, 3875. [[CrossRef](#)]
23. Manouchehrian, A.; Cai, M. Simulation of unstable rock failure under unloading conditions. *Can. Geotech. J.* **2016**, *53*, 22–34. [[CrossRef](#)]
24. Hoxha, D.; Giraud, A.; Homand, F. Modelling long-term behaviour of a natural gypsum rock. *Mech. Mater.* **2005**, *37*, 1223–1241. [[CrossRef](#)]
25. Zhao, Y.L.; Wang, Y.X.; Wang, W.J.; Wan, W.; Tang, J.Z. Modeling of non-linear rheological behavior of hard rock using triaxial rheological experiment. *Int. J. Rock Mech. Min. Sci.* **2017**, *93*, 66–75. [[CrossRef](#)]
26. Zhu, G.A.; Dou, L.M.; Wang, C.B.; Ding, Z.W.; Feng, Z.J. Experimental Study of Rock Burst in Coal Samples under Overstress and True-triaxial Unloading Through Passive Velocity Tomography. *Saf. Sci.* **2019**, *117*, 388–403. [[CrossRef](#)]
27. Zhang, Y.S.; Yu, B.; Zuo, S.Y.; Zheng, K.X.; Li, P.F.; He, X. Experimental and theoretical investigations of dacite under unloading lateral confining stress. *Arab. J. Geosci.* **2021**, *14*, 2659. [[CrossRef](#)]
28. Yang, Y.J.; Zhou, Y.; Ma, D.P.; Ji, H.Y.; Zhang, Y.D. Acoustic Emission Characteristics of Coal under Different Triaxial Unloading Conditions. *Acta Geodyn. Et Geomater.* **2020**, *17*, 51–60. [[CrossRef](#)]
29. Akdag, S.; Karakus, M.; Taheri, A.; Nguyen, G.; He, M.C. Effects of Thermal Damage on Strain Burst Mechanism for Brittle Rocks Under True-Triaxial Loading Conditions. *Rock Mech. Rock Eng.* **2018**, *51*, 1657–1682. [[CrossRef](#)]
30. Liang, Y.P.; Li, Q.M.; Gu, Y.L.; Zou, Q.L. Mechanical and Acoustic Emission Characteristics of Rock: Effect of Loading and Unloading Confining Pressure at The Postpeak Stage. *J. Nat. Gas Sci. Eng.* **2017**, *44*, 54–64. [[CrossRef](#)]
31. Ni, X.H.; Shen, X.M.; Zhu, Z.D. Mechanical and Acoustic Emission Characteristics of Sandstone through Triaxial Unloading Test after Cyclic Freezing-Thawing Treatment. *Adv. Civ. Eng.* **2020**, *2020*, 7150536. [[CrossRef](#)]
32. He, M.C.; Miao, J.L.; Feng, J.L. Rock Burst Process of Limestone and Its Acoustic Emission Characteristics under True-Triaxial Unloading Conditions. *Int. J. Rock Mech. Min. Sci.* **2010**, *47*, 286–298. [[CrossRef](#)]
33. He, M.C.; Zhao, F. Laboratory Study of Unloading Rate Effects on Rockburst. *Disaster Adv.* **2013**, *6*, 11–18.
34. Zhao, X.G.; Wang, J.; Cai, M.; Cheng, C.; Ma, L.K.; Su, R.; Zhao, F.; Li, D.J. Influence of Unloading Rate on the Strainburst Characteristics of Beishan Granite under True-Triaxial Unloading Conditions. *Rock Mech. Rock Eng.* **2014**, *47*, 467–483. [[CrossRef](#)]
35. Hou, G.Y.; Liang, J.P.; Jing, H.Y.; Tan, J.X.; Zhang, Y.K.; Yang, X. Experimental Study on Deformation and Acoustic Emission Characteristics of Arch Roadway under Different Unloading Rates. *Adv. Civ. Eng.* **2020**, *2020*, 8818242. [[CrossRef](#)]
36. Zhang, M.W.; Meng, Q.B.; Liu, S.D.; Qian, D.Y.; Zhang, N. Impacts of Cyclic Loading and Unloading Rates on Acoustic Emission Evolution and Felicity Effect of Instable Rock Mass. *Adv. Mater. Sci. Eng.* **2018**, *2018*, 8365396. [[CrossRef](#)]
37. Meng, Q.B.; Zhang, M.W.; Han, L.J.; Pu, H.; Chen, Y.L. Acoustic Emission Characteristics of Red Sandstone Specimens under Uniaxial Cyclic Loading and Unloading Compression. *Rock Mech. Rock Eng.* **2018**, *51*, 969–988. [[CrossRef](#)]
38. Liang, D.X.; Zhang, N.; Xie, L.X.; Zhao, G.M.; Qian, D.Y. Damage and fractal evolution trends of sandstones under constant-amplitude and tiered cyclic loading and unloading based on acoustic emission. *Int. J. Distrib. Sens. Netw.* **2019**, *15*, 1550147718961020. [[CrossRef](#)]
39. Meng, Q.B.; Chen, Y.L.; Zhang, M.W.; Han, L.J.; Pu, H.; Liu, J.F. On the Kaiser Effect of Rock under Cyclic Loading and Unloading Conditions: Insights from Acoustic Emission Monitoring. *Energies* **2019**, *12*, 3255. [[CrossRef](#)]
40. Zhao, G.M.; Wang, C.; Liang, D.X. Comparative Experimental Studies of Acoustic Emission Characteristics of Sandstone and Mudstone under the Impacts of Cyclic Loading and Unloading. *Int. J. Distrib. Sens. Netw.* **2018**, *14*, 1550147718795552. [[CrossRef](#)]
41. Meng, Q.B.; Zhang, M.W.; Han, L.J.; Pu, H.; Nie, T.Y. Effects of Acoustic Emission and Energy Evolution of Rock Specimens under the Uniaxial Cyclic Loading and Unloading Compression. *Rock Mech. Rock Eng.* **2016**, *49*, 3873–3886. [[CrossRef](#)]
42. Li, D.X.; Wang, E.Y.; Kong, X.G.; Jia, H.S.; Wang, D.M.; Muhammad, A. Damage Precursor of Construction Rocks under Uniaxial Cyclic Loading Tests Analyzed by Acoustic Emission. *Constr. Build. Mater.* **2019**, *206*, 169–178.
43. Zhao, K.; Xiong, L.X.; Xu, Y.D.; Xu, Z.Y.; Zeng, P. Uniaxial Compression Creep and Acoustic Emission Characteristics of Sandstone under Loading-Unloading Paths. *Arab. J. Geosci.* **2020**, *13*, 1243. [[CrossRef](#)]
44. Huang, S.J.; Meng, X.R.; Zhao, G.M.; Li, Y.M.; Liu, G.; Dong, C.L.; Cheng, X.; Xu, W.S.; Liu, C.Y.; Zhou, J. Creep Mechanics of the High-Stress Soft Rock under Grade Unloading. *Adv. Civ. Eng.* **2020**, *2020*, 8822265. [[CrossRef](#)]
45. Hou, Z.Y.; Hao, C.B.; Xiao, F.K.; Liu, G. Research on Energy Conversion and Damage Features of Unloading Instability of Sandstone under High Stress. *Adv. Civ. Eng.* **2021**, *2021*, 6655968. [[CrossRef](#)]
46. Cai, M. Influence of intermediate principal stress on rock fracturing and strength near excavation boundaries—Insight from numerical modeling. *Int. J. Rock Mech. Min. Sci.* **2008**, *45*, 763–772. [[CrossRef](#)]
47. Yang, R.; Ma, D.P.; Yang, Y.J. Experimental Investigation of Energy Evolution in Sandstone Failure during Triaxial Unloading Confining Pressure Tests. *Adv. Civ. Eng.* **2019**, *2019*, 7419752. [[CrossRef](#)]
48. Mu, W.Q.; Wang, D.Y.; Li, L.C.; Yang, T.H.; Feng, Q.B.; Wang, S.X.; Xiao, F.K. Cement flow in interaction rock fractures and its corresponding new construction process in slope engineering. *Constr. Build. Mater.* **2021**, *303*, 124533. [[CrossRef](#)]
49. Sun, X.; Li, E.B.; Han, Y.; Duan, J.L.; Pu, S.S. Experimental Study on the Deformation and Failure Characteristics of Granite under Unloading Paths. *Chin. J. Undergr. Space Eng.* **2020**, *16*, 665–679.

50. Xiao, F.K.; Hou, Z.Y.; He, J.; Liu, G. Mechanical Characteristics and Acoustic Emission Characteristics of Coal Samples under Variable Angle Shear. *J. China Univ. Min. Technol.* **2018**, *47*, 822–829.
51. Yang, Y.J.; Ma, D.P.; Zhou, Y. Experimental Research on Spectrum Signature Eigen of Acoustic Emission of Coal and Sandstone Damage under Triaxial Unloading Confining Pressure. *J. Min. Saf. Eng.* **2019**, *36*, 1002–1008.
52. Lv, J.H. *Chaos Time Series Analysis and Application*; Wuhan University Press: Wuhan, China, 2002. (In Chinese)